1   **1-Methylnicotinamide is an immune regulatory metabolite in human ovarian cancer**

2   Marisa K. Kilgour[1,2], Sarah MacPherson[2], Lauren Zacharias[3], Sarah Keyes[1], Brenna Pauly[1], Bertrand

3   Allard[4], Julian Smazynski[1,2], Peter H. Watson[2,5], John Stagg[4], Brad H. Nelson[1,2,6], Ralph J.

4   DeBerardinis[3,7] & Phineas T. Hamilton[2], Julian J. Lum[1,2]*

5   1.   Department of Biochemistry and Microbiology, University of Victoria, Victoria, BC, Canada

6   2.   Deeley Research Centre, BC Cancer, Victoria, BC, Canada

7   3.   Children's Research Institute, UT Southwestern, Dallas, Texas, US

8   4.   Centre de Recherche du Centre Hospitalier de l'Université de Montréal, Faculté de Pharmacie,

9   Université de Montréal, Institut du Cancer de Montréal, Quebec, Canada

10   5.   Biobanking and Biospecimen Research Services, Deeley Research Centre, BC Cancer, Victoria,

11   British, Columbia, Canada

12   6.   Department of Medical Genetics, University of British Columbia, Vancouver, BC, Canada

13   7.   Howard Hughes Medical Institute, UT Southwestern Medical Center, Dallas, TX, US

14   *Correspondence: jjlum@bccancer.bc.ca

15 **ABSTRACT**

16 **Immune regulatory metabolites are key features of the tumor microenvironment (TME), yet with**

17 **a few notable exceptions, their identities remain largely unknown. We uncovered the immune**

18 **regulatory metabolic states and metabolomes of sorted tumor and stromal, CD4+, and CD8+ cells**

19 **from the tumor and ascites of patients with high-grade serous ovarian cancer (HGSC) using high-**

20 **dimensional flow cytometry and metabolomics supplemented with single cell RNA sequencing.**

21 **Flow cytometry revealed that tumor cells show a consistently greater uptake of glucose than T**

22 **cells, but similar mitochondrial activity. Cells within the ascites and tumor had pervasive**

23 **metabolite differences, with a striking enrichment in 1-methylnicotinamide (MNA) in T cells**

24 **infiltrating the tumor compared to ascites. Despite the elevated levels of MNA in T cells, the**

25 **expression of nicotinamide N-methyltransferase, the gene encoding the enzyme that catalyses the**

26 **transfer of a methyl group from S-adenosylmethionine to nicotinamide, was restricted to**

27 **fibroblasts and tumor cells. Treatment of T cells with MNA resulted in an increase in T cell-**

28 **mediated secretion of the tumor promoting cytokine tumor necrosis factor alpha. Thus, the TME-**

29 **derived metabolite MNA contributes to an alternative and non-cell autonomous mechanism of**

30 **immune modulation of T cells in HGSC. Collectively, uncovering the tumor-T cell metabolome**

31 **may reveal metabolic vulnerabilities that can be exploited using T cell-based immunotherapies to**

32 **treat human cancer.**

33 Tumor-derived metabolites can have profound suppressive effects on anti-tumor immunity, with

34 increasing evidence that they can also function as key drivers of disease progression[1,2]. Beyond the

35 Warburg effect, recent work has begun to characterize the metabolic states of tumor cells and their

36 relationship to the immunological state of the TME. Studies in murine models have helped uncover the

37 role of metabolites such as (R)-2-hydroxyglutarate[3], BH4[4] and methylglyoxal[5] as well as pathways

38 including glutamine metabolism[6], oxidative metabolism[7], and glucose metabolism[8] that impact T cell

39 function and antitumor immunity. Furthermore, studies in humans have elucidated key metabolic

40 pathways in tumors, for example demonstrating that tumors can use lactate as fuel[9]. Despite this, the

41 diversity and impact of specific metabolites on tumor-infiltrating lymphocytes (TILs) are largely

42 unknown. To characterize this diversity and better understand how metabolites in the TME influence T

43 cell function, a combined flow cytometry and mass-spectrometry approach was used to profile tumor

44 and TIL from patients with HGSC. Using this approach two spatially distinct microenvironments were

45 interrogated, the ascites[10] and tumor, within the same patients to reveal potential reciprocal metabolic

46 interactions between tumor cells and TIL.

47

48 The phenotypic and metabolic states of cells in the matched ascites and tumor environments from six

49 patients with HGSC (Extended Data Table 1) were evaluated using high-dimensional flow cytometry to

50 synchronously quantify glucose uptake (2-(N-(7-Nitrobenz-2-oxa-1,3-diazol-4-yl)Amino)-2-

51 Deoxyglucose, 2-NBDG) and mitochondrial activity (MitoTracker Deep Red)[5,11,12] alongside canonical

52 markers to distinguish immune and tumor cell populations (Extended Data Table 2, Extended Data Fig.

53 1a). This revealed high levels of glucose uptake in tumor cells relative to T cells in both the ascites and

54 tumor, but more modest differences in mitochondrial activity. Tumor cells (CD45-EpCAM+) had on

55 average 3-4 times the glucose uptake of T cells, whereas CD4+ T cells had on average 1.2 times the

56 glucose uptake of CD8+ T cells, suggesting that TILs have different metabolic requirements even within

57   the same TME (Fig. 1a). In contrast, the mitochondrial activity in tumor cells was similar to CD4+ T

58   cells, and both had greater mitochondrial activity than CD8+ T cells (Fig. 1b). Collectively, these results

59   reveal a metabolic hierarchy, with tumor cells more active than CD4+ T cells, and CD4+ T cells more

60   metabolically active than CD8+ T cells. Despite these effects across cell types, there were no consistent

61   differences in the metabolic states of CD4+ and CD8+ T cells, or their relative proportions, in the ascites

62   compared to the tumor (Fig. 1c). Conversely, within the CD45- cell fraction, there was an increase in the

63   proportion of EpCAM+ cells in the tumor compared to the ascites (Extended Data Fig. 1b). We also

64   observed clear metabolic differences among EPCAM+ and EPCAM- cell fractions. EPCAM+ (tumor)

65   cells had substantially greater glucose uptake and mitochondrial activity than EPCAM- cells, consistent

66   with much higher metabolic activity in tumor cells than fibroblasts in the TME (Extended Data Fig. 1c,

67   d).

68

69   Further analysis revealed other clear differences when considering more highly-resolved phenotypic

70   states of T cells[13]. Indeed, activated (Extended Data Fig. 1e-g) and effector memory (Extended Data Fig.

71   1h, i) T cells were much more frequent (as a proportion of T cells) in the tumor than ascites. Similarly,

72   resolving phenotypes by the expression of activation markers (PD1, CD25, CD137) revealed that while

73   these populations showed some differences in metabolism (Extended Data Fig. 2a-e), no consistently

74   significant metabolic differences were observed between naïve, effector, or memory cells (defined by

75   CCR7 and CD45RO, Extended Data Fig. 2f-i). These results were confirmed through automated

76   assignment of cell phenotypes using machine learning method[14], which further revealed an abundant

77   myeloid cell population (CD3-/CD4+) predominately in patient ascites that displayed the highest

78   glucose uptake and mitochondrial activity of any identified cell type (Extended Data Fig 3). These

79   results underscore strong metabolic differences across different cell types found in the ascites and

80   tumors of HGSC patients.

81   A major challenge in understanding the metabolomic profiles of TIL has been the need to isolate

82   samples of T cells of sufficient purity, quality and quantity from tumors. Recent studies have shown that

83   flow cytometry based sorting and bead enrichment methods can cause alterations in cellular metabolite

84   profiles[15–17]. To overcome this, we optimized a bead enrichment approach to isolate and separate TIL

85   from surgically resected human ovarian cancers prior to analysis by liquid chromatography tandem mass

86   spectrometry (LC-MS/MS) (See Methods; Extended Data Fig. 4a). To assess the overall impact of this

87   protocol on metabolite changes, we compared the metabolite profiles of activated T cells following bead

88   isolation to cells that did not undergo bead isolation but remained on ice, and found high correlation

89   among methods ($r = 0.77$), as well as high reproducibility among technical replicates for this panel of 86

90   metabolites (see Extended Data Fig. 4b). These methods thus enabled accurate metabolite profiling in

91   cells undergoing enrichment, to provide a first high-resolution platform for the identification of specific

92   metabolites in HGSC thereby allowing deeper insight into cell-specific metabolic programs.

93

94   We applied this enrichment method to profile 99 metabolites in CD4+, CD8+, and CD45- cell fractions

95   from the primary ascites and tumor of six patients with HGSC (Extended Data Fig. 4c). Profiling

96   revealed strong metabolic separation of cell types within and across patients (Fig. 2a, Extended Data

97   Fig. 5a). In particular, patient 70 had distinct metabolic profiles compared to other patients (Fig. 2b,

98   Extended Data Fig. 5b), indicating the potential for substantial metabolic heterogeneity among patients.

99   Notably, patient 70 had a smaller total volume of ascites collected (80 mL) compared to the other

100 patients (1.2-2 L) (Extended Data Table 1). Controlling for inter-patient heterogeneity during principal

101 component analysis (e.g. using partial redundancy analysis) revealed consistent changes among cell

102 types, with clear clustering of cell types and/or microenvironments based on metabolite profile (Fig. 2c).

103 Analyses of single metabolites underscored these effects and revealed dramatic differences among cell

104 types and microenvironments. Notably, the most extreme difference observed was for 1-

105   methylnicotinamide (MNA), which was enriched in CD45- cells in general, and ~10-100-fold in T cells

106   when they infiltrated the tumor (Fig. 3a). This effect was most pronounced for CD4+ T cells; while

107   MNA in CD8+ cells also appeared to be strongly affected by the environment, this was not significant as

108   tumor CD8+ fractions were only evaluable for three of the six patients.

109

110   MNA is produced by the transfer of a methyl group from s-adenosyl-L-methionine (SAM) to

111   nicotinamide (NA) by nicotinamide N-methyltransferase (NNMT). *NNMT* is over-expressed in multiple

112   human cancers and has been linked to proliferation, invasion, and metastasis. To better understand the

113   source of MNA in T cells in the TME, we used single cell RNA sequencing (scRNA-seq) to characterize

114   *NNMT* expression across cell types in the ascites and tumor of three patients with HGSC (Extended Data

115   Table 3). Profiling ~6,500 cells revealed that *NNMT* expression was confined to presumptive fibroblast

116   and tumor cell populations in both the ascites and tumor environments (Fig. 3b,c). Notably, there was no

117   appreciable *NNMT* expression in any *PTPRC*-expressing (CD45+) populations (Fig. 3c), suggesting the

118   MNA detected in metabolite profiling is imported into T cells. The expression of aldehyde oxidase 1

119   (*AOX1),* which converts MNA to 1-methyl-2-pyridone-5-carboxamide (2-PYR) or 1-methyl-4-pyridone-

120   5-carboxamide (4-PYR), was likewise restricted to fibroblast populations (Extended Data Fig. 6),

121   collectively suggesting that T cells lack the capacity for conventional MNA metabolism. This metabolite

122   profile and scRNA-seq analysis also revealed similar, although less dramatic, patterns for both L-

123   kynurenine and adenosine (Extended Data Fig. 7), two well-characterized immunosuppressive

124   metabolites that were also elevated in T cells from the tumor, and/or in tumor cells. These trends,

125   coupled with the striking enrichment of MNA in T cells within the tumor, raised the possibility that

126   secretion of MNA into the TME may modulate the phenotypes of TIL to compromise antitumor

127   immunity.

128   To determine the impact of MNA on T cells, healthy donor T cells were activated in the presence of

129   MNA and assessed for proliferation and function. Addition of MNA did not lead to decreased

130   proliferation or viability in either CD4+ or CD8+ T cells after 7 days (Fig. 4a), but rather increased the

131   proportion of CD4+ and CD8+ T cells that expressed tumor necrosis factor alpha (TNFα) (Fig. 4b).

132   While TNFα has been reported to have context-dependent pro- and anti-tumor effects, it has a well-

133   described role in promoting ovarian cancer growth and metastasis[18–20]. Patients with ovarian cancer have

134   been reported to have higher concentrations of TNFα within their ascites and tumor tissue than selected

135   benign tissue[21–23]. Mechanistically, TNFα can modulate activation, function and proliferation of

136   leukocytes, and change the phenotype of cancer cells[24,25]. Consistent with these findings, differential

137   expression analysis of T cell populations between the ascites and tumor also revealed a significant up-

138   regulation of *TNF* on T cells in the tumor relative to the ascites. Importantly, the increase in *TNF* was

139   only apparent for T cell populations that did not exhibit a cytotoxic phenotype (Fig. 4c). Taken together,

140   these data support the notion of a dual immune suppressive and tumor promoting role for MNA in

141   HGSC.

142

143   By applying a combined metabolomics approach, this study revealed pervasive immune metabolome

144   differences between cells within the tumor and ascites of HGSC patients. This integrated analysis

145   demonstrated differences in glucose uptake and mitochondrial activity between T cells and tumor cells

146   in HGSC. However, these flow-based methods of assessing metabolism, while methodologically

147   straightforward and providing single cell resolution, do not provide sufficient information regarding the

148   cellular impacts of specific metabolites that function in cis or in trans within a given cell type.

149   Importantly, our work uncovered a previously unrecognized metabolite MNA as differentially abundant

150   between compartments and cell types. *In vitro*, MNA increased T cell-mediated secretion of the tumor

151   promoting cytokine TNFα, providing insight for an alternative and non-cell autonomous role of MNA as

152   an immune modulator in the ovarian TME.

References

1. Allard, B., Beavis, P. A., Darcy, P. K. & Stagg, J. Immunosuppressive activities of adenosine in cancer. *Curr. Opin. Pharmacol.* **29**, 7–16 (2016).

2. Labadie, B. W., Bao, R. & Luke, J. J. Reimagining IDO Pathway Inhibition in Cancer Immunotherapy via Downstream Focus on the Tryptophan–Kynurenine–Aryl Hydrocarbon Axis. *Clin. Cancer Res.* **25**, 1462–1471 (2019).

3. Bunse, L. *et al.* Suppression of antitumor T cell immunity by the oncometabolite (R)-2-hydroxyglutarate. *Nat. Med.* **24**, 1192–1203 (2018).

4. Cronin, S. J. F. *et al.* The metabolite BH4 controls T–cell proliferation in autoimmunity and cancer. *Nature* **563**, 564–568 (2018).

5. Baumann, T. *et al.* Regulatory myeloid cells paralyze T cells through cell–cell transfer of the metabolite methylglyoxal. *Nat. Immunol.* **21**, 555–566 (2020).

6. Leone, R. D. *et al.* Glutamine blockade induces divergent metabolic programs to overcome tumor immune evasion. *Science* **366**, 1013–1021 (2019).

7. Najjar, Y. G. *et al.* Tumor cell oxidative metabolism as a barrier to PD-1 blockade immunotherapy in melanoma. *JCI Insight* **4**, (2019).

8. Chang, C.-H. *et al.* Metabolic Competition in the Tumor Microenvironment Is a Driver of Cancer Progression. *Cell* **162**, 1229–1241 (2015).

9. Faubert, B. *et al.* Lactate metabolism in human lung tumors. *Cell* **171**, 358-371.e9 (2017).

10. Kipps, E., Tan, D. S. P. & Kaye, S. B. Meeting the challenge of ascites in ovarian cancer: new avenues for therapy and research. *Nat. Rev. Cancer* **13**, 273–282 (2013).

11. Scharping, N. E. *et al.* The Tumor Microenvironment Represses T Cell Mitochondrial Biogenesis to Drive Intratumoral T Cell Metabolic Insufficiency and Dysfunction. *Immunity* **45**, 374–388 (2016).

12. Ho, P.-C. *et al.* Phosphoenolpyruvate Is a Metabolic Checkpoint of Anti-tumor T Cell Responses.

177   *Cell* **162**, 1217–1228 (2015).

178   13. Rådestad, E. *et al.* Immune profiling and identification of prognostic immune-related risk factors in

179   human ovarian cancer. *OncoImmunology* **8**, e1535730 (2019).

180   14. Greene, E. *et al.* New interpretable machine learning method for single-cell data reveals correlates of

181   clinical response to cancer immunotherapy. *bioRxiv* 702118 (2019) doi:10.1101/702118.

182   15. Ma, E. H. *et al.* Metabolic Profiling Using Stable Isotope Tracing Reveals Distinct Patterns of

183   Glucose Utilization by Physiologically Activated CD8+ T Cells. *Immunity* **51**, 856-870.e5 (2019).

184   16. Binek, A. *et al.* Flow Cytometry Has a Significant Impact on the Cellular Metabolome. *J. Proteome*

185   *Res.* **18**, 169–181 (2019).

186   17. Llufrio, E. M., Wang, L., Naser, F. J. & Patti, G. J. Sorting cells alters their redox state and cellular

187   metabolome. *Redox Biol.* **16**, 381–387 (2018).

188   18. Kulbe, H. *et al.* The inflammatory cytokine tumor necrosis factor-alpha generates an autocrine

189   tumor-promoting network in epithelial ovarian cancer cells. *Cancer Res.* **67**, 585–592 (2007).

190   19. Charles, K. A. *et al.* Infliximab, a humanised anti-TNF-a monoclonal antibody, exhibits biological

191   activity in the ovarian tumor microenvironment in patients. *Cancer Res.* **66**, 1055–1056 (2006).

192   20. Salako, M. A. *et al.* Inhibition of the Inflammatory Cytokine TNF-α Increases Adenovirus Activity

193   in Ovarian Cancer via Modulation of cIAP1/2 Expression. *Mol. Ther.* **19**, 490–499 (2011).

194   21. Sipak-Szmigiel, O. *et al.* Serum and peritoneal fluid concentrations of soluble human leukocyte

195   antigen, tumor necrosis factor alpha and interleukin 10 in patients with selected ovarian pathologies.

196   *J. Ovarian Res.* **10**, 25 (2017).

197   22. Szlosarek, P. W. *et al.* Expression and regulation of tumor necrosis factor alpha in normal and

198   malignant ovarian epithelium. *Mol. Cancer Ther.* **5**, 382–390 (2006).

199   23. Piura, B. *et al.* Distinct Expression and Localization of TNF System in Ovarian Carcinoma Tissues:

200   Possible Involvement of TNF-α in Morphological Changes of Ovarian Cancerous Cells. *Anticancer*

201   *Res.* **34**, 745–752 (2014).

202   24. Montfort, A. *et al.* The TNF Paradox in Cancer Progression and Immunotherapy. *Front. Immunol.*

203   **10**, (2019).

204   25. Charles, K. *et al.* The tumor-promoting actions of TNF-α involve TNFR1 and IL-17 in ovarian

205   cancer in mice and humans. *J. Clin. Invest.* **119**, 3011–23 (2009).

206 **Figures**
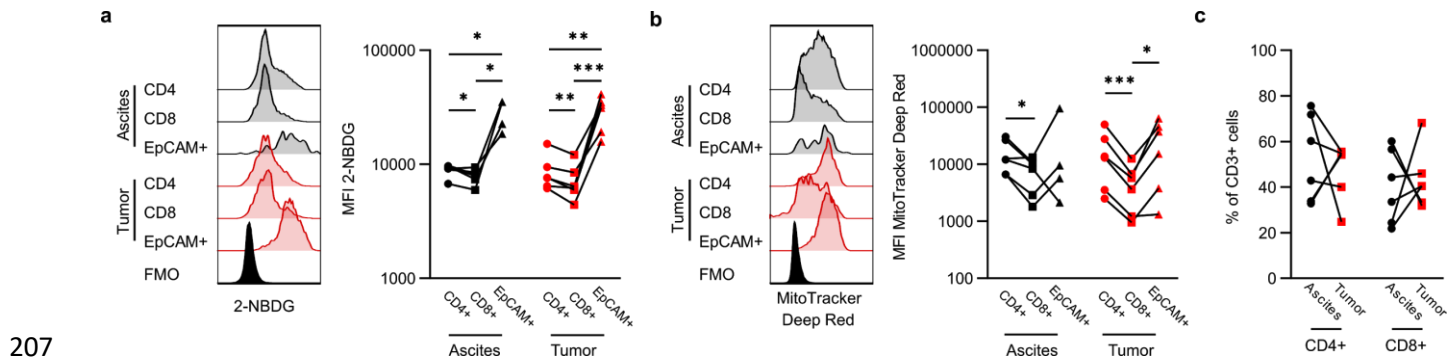
208 **Figure 1 | Tumor cells have greater glucose uptake but similar mitochondrial activity to T cells. a**,

209 **b**, Representative plot (left) and tabulated data (right) for median fluorescent intensity (MFI) of glucose

210 uptake (2-NBDG) (**a**) and mitochondrial activity (MitoTracker Deep Red) (**b**) of CD4+ T cells, CD8+ T

211 cells, and EpCAM+CD45- tumor cells from ascites and tumor. **c**, Proportion of CD4+ and CD8+ cells

212 (of CD3+ T cells) within ascites and tumor. P-values determined by paired t-test (*p<0.05, **p<0.01,

213 ***p<0.001) (**a-c**). Lines indicate matched patients (n=6). Fluorescence Minus One (FMO); Median

214 Fluorescence Intensity (MFI).

215

216
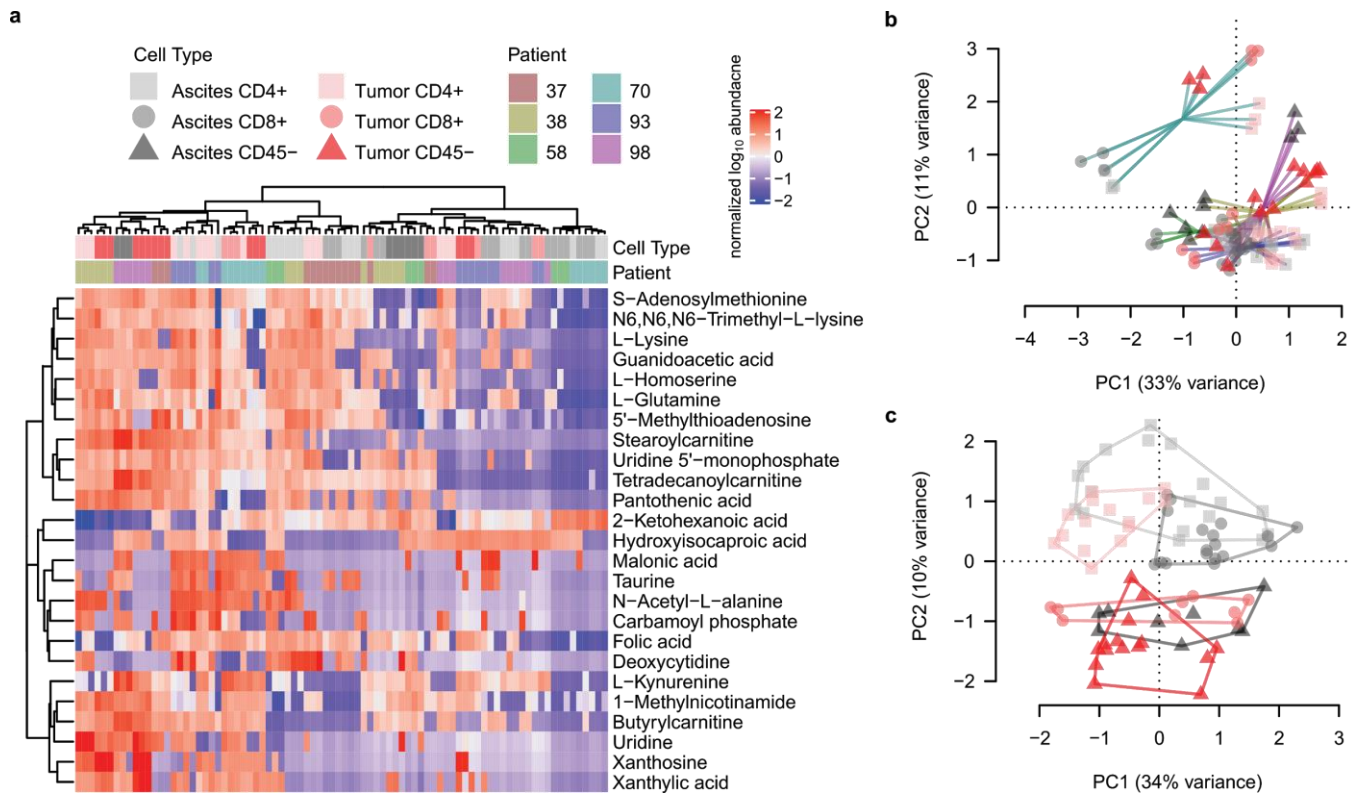
Figure 2 | Metabolite profiling of matched ascites and tumor reveals key differences between tumor cells and T cells. a, Heatmap of normalized metabolite abundance, with dendrograms representing Ward's clustering of Euclidean distances among samples. **b**, Principal components analysis (PCA) of sample metabolite profiles, showing triplicate replicates of each sample, with samples from the same patients joined by lines. **c**, PCA of sample metabolite profiles conditioned on patient (i.e. using partial redundancy); sample types are circumscribed by convex hulls.

223

224
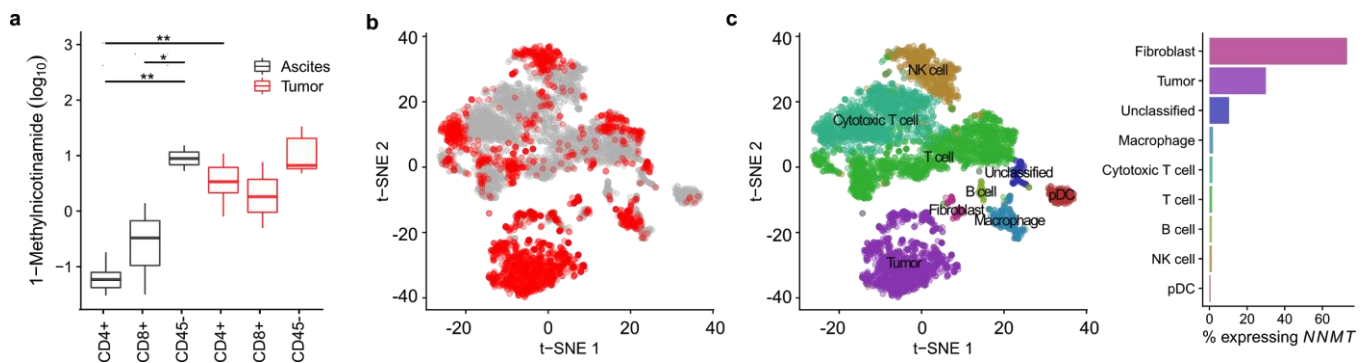
Figure 3 | 1-Methylnicotinamide (MNA) is more abundant in T cells from the tumor compared to ascites. a, Normalized abundance of MNA in CD4+, CD8+ and CD45- cells from ascites and tumor. Boxplots show medians (lines), interquartile range (box hinges) and range of data up to 1.5X interquartile range (box whiskers). P-values are determined using *limma* with patient as a random effect, as described in methods (*p<0.05, **p<0.01). **b**, t-SNE of scRNA-seq of ascites (grey) and tumor (red) (n=3 patients). **c**, *NNMT* expression in different cellular populations identified using scRNA-seq.

231

232
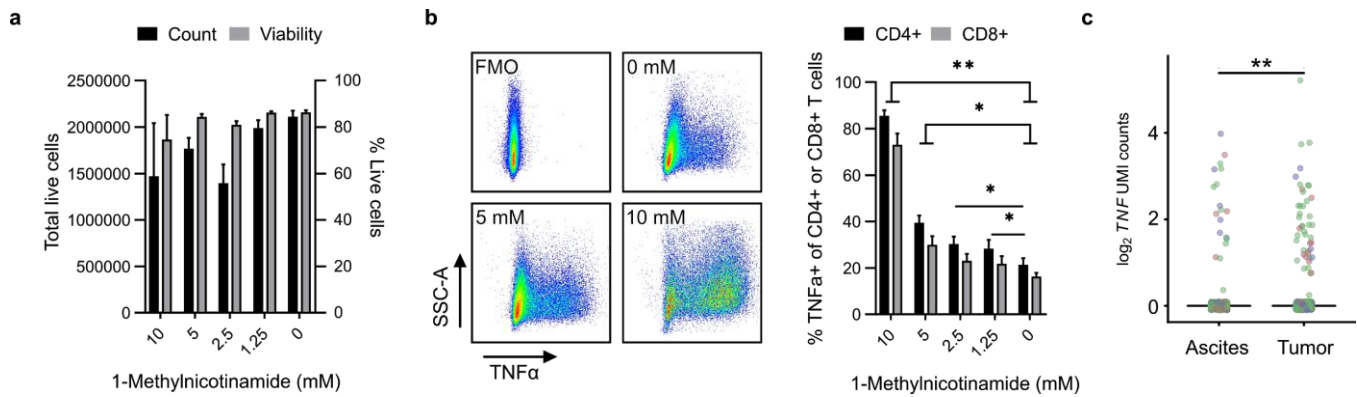
Figure 4 | Exogenous MNA enhances TNFα expression in T cells. a, Total live cell count and viability directly from culture on day 7. Bar graphs represent mean with SEM of three healthy donors. **b,** TNFα expression in T cells treated with exogenous MNA. T cells were activated using CD3/CD28 with IL2 in respective concentrations of MNA for 7 days. Cells were stimulated with PMA/Ionomycin with GolgiStop^{TM} for 4 hours prior to analysis. Example plot of live cells (left) and tabulated data (right). Bar graphs represent mean with SEM of 3 healthy donors. P-value determined using paired t-test (*p<0.05, **p<0.01). **c,** T cells (non-cytotoxic) show increased expression of *TNF* in the tumor relative to the ascites of HGSC. Colors represent different patients. Displayed cells have been randomly subsampled to 300 and jittered to limit overplotting (P_{adj} = 0.0076).

Methods

Patient sample collection and processing. Patient specimens and clinical data were obtained through

the BC Cancer Tumour Tissue Repository (TTR), certified by the Canadian Tissue Repository Network.

All specimens and clinical data were obtained with either informed written consent or a formal waiver of

consent under protocols approved by the Research Ethics Board of the BC Cancer Agency and the

University of British Columbia (H07-00463). Samples are stored in a certified BioBank (BRC-00290).

Detailed patient characteristics are shown in **Extended Data Table 1** and **Extended Data Table 3**.

For cryopreservation, patient tumor samples were mechanically disaggregated using a scalpel

and pushed through a 100 μm filter to obtain a single cell suspension. Patient ascites was centrifuged at

1500 rpm for 10 minutes at 4 °C to pellet cells and remove supernatant. Cells obtained from tumor and

ascites were cryopreserved in 50% heat inactivated human AB serum (Sigma), 40% RPMI-1640 (Fisher)

and 10% DMSO.

Cell culture reagents. Complete media consisted of a 0.22 μm filtered 50:50 supplemented

RPMI1640:AimV. RPMI1640 + 2.05 mM L-Glutamine (Fisher) was supplemented with 10% heat

inactivated human AB serum (Sigma), 12.5 mM HEPES (Fisher), 2 mM L-Glutamine (Fisher), 1x

Penicillin Streptomycin solution (Fisher) and 50 μM B-mercaptoethanol. AimV (Invitrogen) was

supplemented with 20 mM HEPES (Fisher) and 2 mM L-glutamine (Fisher). Flow cytometry staining

buffer consisted of 0.22 μm filtered PBS (Invitrogen) supplemented with 3% heat inactivated AB human

serum (Sigma). Cell enrichment buffer consisted of 0.22 μm filtered PBS supplemented with 0.5% heat

inactivated human AB serum (Sigma).

Flow cytometry for metabolic profiling. Cells were stained with 10 nM MitoTracker Deep Red (MT

DR) and 100 μM 2-(N-(7-Nitrobenz-2-oxa-1,3-diazol-4-yl)Amino)-2-Deoxyglucose (2-NBDG) for 30

minutes in complete media at 37°C. Next, cells were stained with viability dye-eF506 for 15 minutes at

4 °C. Cells were resuspended in F_C block (eBioscience) and Brilliant Stain Buffer (BD Bioscience)

266   diluted in flow cytometry staining buffer (according to manufacturer instructions) and incubated for 10

267   minutes at room temperature. Cells were stained with a panel of antibodies (**Extended Data Table 3**) in

268   flow cytometry staining buffer for 20 minutes at 4 °C. Cells were resuspended in flow cytometry

269   staining buffer prior to analysis (Cytek Aurora; 3L-16V-14B-8R configuration).

270   Cytometry data were analyzed using SpectroFlo and FlowJo V10, and figures were created using

271   GraphPad Prism 8. Median Fluorescent Intensity of 2-NBDG and MT DR were $\log_{10}$ normalized prior to

272   statistical analysis using paired t-test to account for matched patients. Any population with less than 40

273   events was removed from the analysis, an MFI value of 1 was inputted for any negative values prior to

274   statistical analysis and data visualization.

275   **Unbiased discovery of cell populations in flow cytometry data.** To supplement our manual gating

276   strategy for the above flow panel, we used Full Annotation Using Shape-constrained Trees (FAUST)[14]

277   to automatically assign cells to populations, after dead cell exclusion in FlowJo. We manually curated

278   outputs to merge populations that appeared to be mis-assigned (merged PD1+ with PD1- tumor cells),

279   and retained populations comprising, on average, more than 2% of cells in each sample, for a total of 11

280   populations.

281   **Cell activation and enrichment for metabolite profiling optimization.** Peripheral blood mononuclear

282   cells (PBMCs) were isolated from a Leukopheresis Pack (Stemcell) using Ficoll gradient density

283   centrifugation. CD8+ T cells were isolated from the PBMCs using CD8 MicroBeads (Miltenyi) and

284   expanded using TransAct (Miltenyi) for 2 weeks in complete media according to manufacturer's

285   instructions. Cells were rested for 5 days in complete media with 10 ng/ml IL-7 (Peprotech) and then

286   restimulated with TransAct. On day 7, cells were enriched using CD45 MicroBeads (Miltenyi) in three

287   rounds of sequential enrichment according to the manufacturer's instructions. Cells were aliquoted for

288   analysis by flow cytometry (described above) and 1 million cells were aliquoted in triplicate for analysis

289   by LC-MS/MS. Samples were processed for LC-MS/MS as described below. We imputed missing

290   metabolite values with an ion count of 1000. Each sample was normalized by total ion count (TIC) and

291    $\log_{10}$ transformed prior to statistical analysis.

292   **Cell-type enrichment of patient samples.** Patient cells were filtered through a 40 μm filter. Samples

293   were enriched for CD8+, CD4+ and CD45- cells (on ice) using three sequential rounds of positive

294   selection by magnetic bead separation (Miltenyi MACS MicroBeads). CD8- fraction was used for CD4

295   enrichment, and the CD4- fraction was used for CD45- enrichment to maximize cell recovery.

296   **LC-MS/MS metabolite profiling.** To prepare samples (in triplicate) for metabolite profiling, cells were

297   washed once with ice-cold saline solution and 1 mL of 80% methanol added to each sample before

298   vortexing and snap freezing in liquid nitrogen. Samples were subjected to 3 freeze-thaw cycles, and

299   centrifuged at 14,000 rpm for 15 minutes at 4 °C. The metabolite-containing supernatant was evaporated

300   until dry. Metabolites were reconstituted in 50 μl of 0.03% formic acid, vortex-mixed, and centrifuged to

301   remove debris. The supernatant was transferred to a high-performance liquid chromatography (HPLC)

302   vial for the metabolomics study. Each sample was processed with similar numbers of cells using a

303   randomized processing scheme to prevent batch effects. We performed qualitative assessment of global

304   metabolites as previously published on the AB SCIEX QTRAP 5500 triple-quadrupole mass

305   spectrometer[26]. Chromatogram review and peak area integration were performed using MultiQuant

306   software version 2.1 (Applied Biosystems SCIEX).

307   **Characterizing metabolic differences across cell types and microenvironments.** Missing metabolite

308   values were imputed with an ion count of 1000 and normalized peak area calculated for each detected

309   metabolite using the total ion count from each sample to correct variations introduced from sample

310   handling through instrument analysis. TIC-normalization was followed by $\log_{10}$ transformation and

311   autoNorm row-scaling using *MetaboAnalystR*[27] (default parameters). We conducted exploratory analysis

312   of metabolome differences across sample types using PCA with the *vegan* R package, and conditioned

313   the analysis on patient using partial redundancy analysis. Heatmap dendrograms were constructed using

314 Ward's method to cluster Euclidean distances among samples. We identified differentially-abundant

315 metabolites across cell types and microenvironments using *limma*[28] on the $\log_{10}$-transformed row-

316 normalized metabolite abundances. To simplify interpretation, we specified the model using the group

317 means parameterization, treating cell types within microenvironments as each group (n=6 groups); for

318 significance testing we took the average of triplicate measurements for each metabolite to avoid

319 pseudoreplication, and included patient as a block in the *limma* design. To examine metabolites that

320 differed across patients we re-fit models in *limma* including patient as a fixed effect. We reported

321 significance at $P_{adj} < 0.05$ (Benjamini-Hochberg correction) for pre-specified contrasts among cell types

322 and microenvironments.

323 **scRNA-seq.** Single cell transcriptome sequencing was performed on total viably-frozen ascites and

324 tumor samples using the 10X 5' Gene Expression protocol, following viability enrichment with the

325 Miltenyi Dead Cell Removal Kit (>80% viability). 5 cases with matched tumor and ascites available

326 were profiled, although low viability from 1 tumor sample prevented its inclusion. To enable

327 multiplexing of patients, we combined samples from each patient in lanes of the 10X Chromium

328 controller, with separate runs for ascites and tumor fractions. Following sequencing (Illumina HiSeq

329 4000 26x98bp PE, Genome Quebec; mean of 73,488 and 41,378 reads per cell for tumor and ascites,

330 respectively), we assigned donor identities using *CellSNP* and *Vireo*[29] (based on the common human

331 SNP VCF provided by *CellSNP* for GRCh38). We excluded unassigned cells and those identified as

332 doublets, and matched donors between ascites and tumor samples based on the nearest identity-by-state

333 (IBS) of inferred patient genotypes using *SNPRelate*[30]. Based on this assignment, we retained 3 cases

334 with abundant cellular representation in both tumor and ascites fractions for downstream analysis.

335 Following quality filtering steps in the *scater*[31] and *scran*[32] BioConductor packages, this yielded 6,975

336 cells (2,792 and 4,183 from tumor and ascites, respectively) for analysis. We clustered cells by

337 expression using *igraph*'s[33] Louvain clustering implementation of the shared nearest neighbour network

338 (SNN) based on Jaccard distance. Clusters were manually annotated into presumptive cell types based

339 on marker gene expression and visualized with t-SNE.

340 **T cell functional assay.** PBMCs were isolated from a leukapheresis product (Stemcell) by Ficoll

341 gradient density centrifugation. CD3+ cells were isolated from the PBMCs using CD3 Microbeads

342 (Miltenyi). The CD3+ cells were activated with plate bound CD3 (5 μg/ml), soluble CD28 (3 μg/ml),

343 and IL-2 (300 U/ml, Proleukin) in the presence or absence of MNA. On the final day of expansion

344 viability (Fixable Viability Dye eFluor450, eBioscience) and proliferation (123count eBeads, Thermo)

345 was assessed by flow cytometry. Effector function was assessed by stimulating cells for 4 hours with

346 PMA (20 ng/ml) and Ionomycin (1 μg/ml) with GolgiStopTM and monitored for CD8-PerCP (RPA-T8,

347 Biolegend), CD4-AF700 (RPA-T4, Biolegend), and TNFa-FITC (MAb11, BD).

348 **Statistical analysis.** Statistical analysis was carried out as described in the text or methods using

349 GraphPad Prism 8, Microsoft Excel or R v3.6.0. Where multiple samples were taken from the same

350 patient (e.g. ascites and tumor), we used paired t-tests, or included patient as a random effect in linear or

351 generalized models, as appropriate. For metabolomic analysis, significance testing was done on means

352 of triplicate measurements.

353 **Data Availability**

354 Raw sequencing data will be deposited at NCBI dbGAP (Accession pending). Processed data files and

355 scripts to reproduce metabolomics and scRNA-seq analyses are available at

356 github.com/vicDRC/onecarbon. Flow cytometry data will be deposited at flowrepository.

357 **Code Availability**

358 R scripts to reproduce metabolomic and single cell RNA-seq analyses are available at

359 github.com/vicDRC/onecarbon.

Methods References

26. Mullen, A. R. *et al.* Oxidation of alpha-ketoglutarate is required for reductive carboxylation in cancer cells with mitochondrial defects. *Cell Rep.* **7**, 1679–1690 (2014).

27. Chong, J. & Xia, J. MetaboAnalystR: an R package for flexible and reproducible analysis of metabolomics data. *Bioinforma. Oxf. Engl.* **34**, 4313–4314 (2018).

28. Ritchie, M. E. *et al.* limma powers differential expression analyses for RNA-sequencing and microarray studies. *Nucleic Acids Res.* **43**, e47–e47 (2015).

29. Huang, Y., McCarthy, D. J. & Stegle, O. Vireo: Bayesian demultiplexing of pooled single-cell RNA-seq data without genotype reference. *Genome Biol.* **20**, 273 (2019).

30. Zheng, X. *et al.* A high-performance computing toolset for relatedness and principal component analysis of SNP data. *Bioinformatics* **28**, 3326–3328 (2012).

31. McCarthy, D. J., Campbell, K. R., Lun, A. T. L. & Wills, Q. F. Scater: pre-processing, quality control, normalization and visualization of single-cell RNA-seq data in R. *Bioinformatics* **33**, 1179–1186 (2017).

32. Lun, A. T. L., Bach, K. & Marioni, J. C. Pooling across cells to normalize single-cell RNA sequencing data with many zero counts. *Genome Biol.* **17**, 75 (2016).

33. Csardi, G. & Nepusz, T. The Igraph Software Package for Complex Network Research. *InterJournal Complex Systems*, 1695 (2005).

Acknowledgements

Author Contributions

M.K.K. and P.T.H. designed and performed experiments, analyzed the data, and wrote the manuscript. S.M., S.K., and B.P. helped perform the metabolite profiling experiments. P.T.H., J.S, B.A., J.S, and B.H.N. generated the scRNA-seq data. L.Z. and R.J.D. generated and analyzed the LC-MS/MS data. P.H.W. oversaw biospecimen collection through the IROC-TTR. J.J.L. conceived the project and wrote the manuscript.

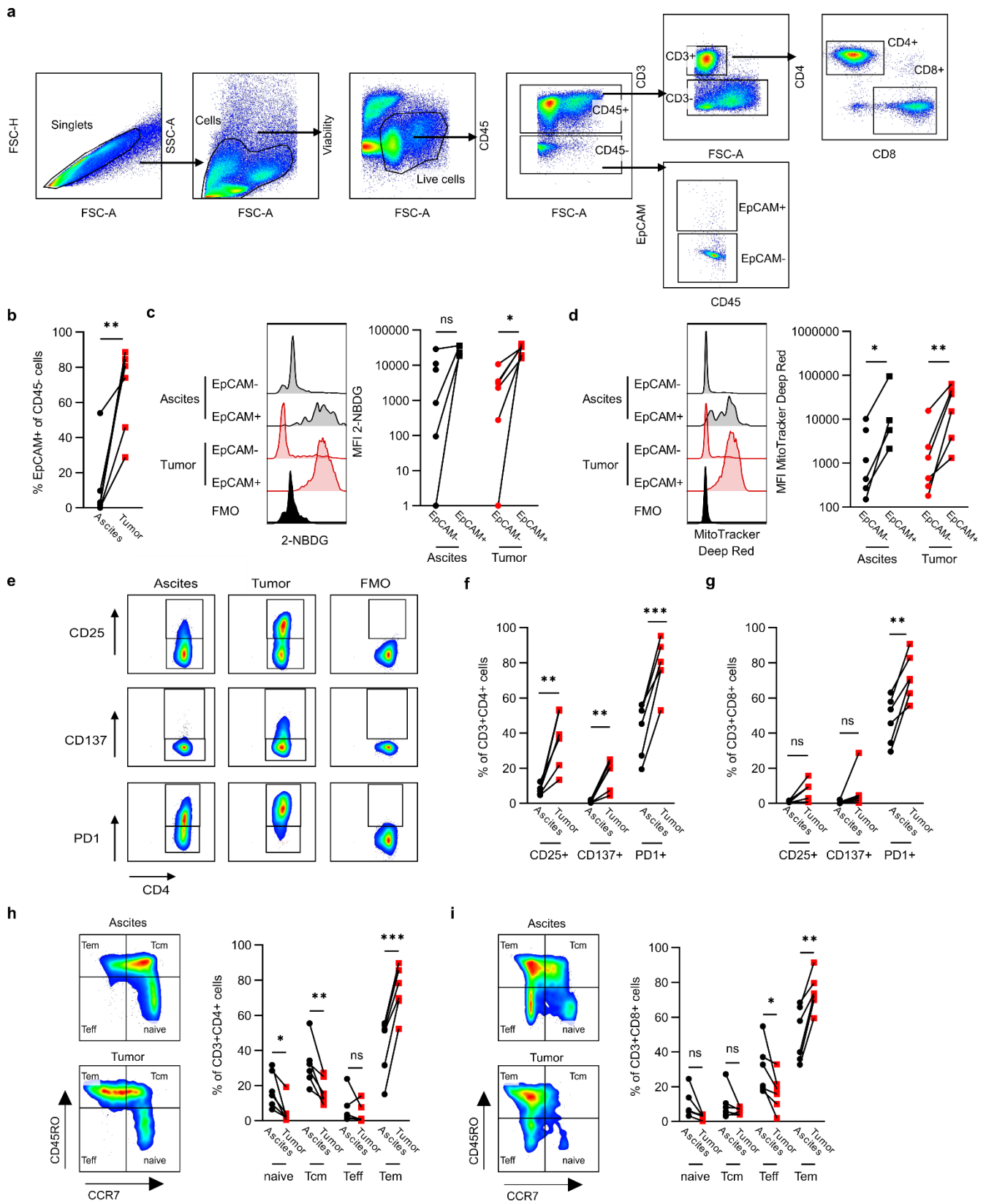**Competing Interests Statement**

J.S. is a permanent member and owns stocks of Surface Oncology. R.J.D is a member of the Scientific Advisory Board at Agios Pharmaceuticals.

Corresponding Author

Correspondence to Julian J. Lum.

399 **Extended data**

401 **Extended Data Figure 1 | Phenotypic characterization of ascites and tumor by flow cytometry. a**,

402 Representative gating strategy for analysis by flow cytometry. **b**, Proportion of EpCAM+ (of CD45-)

403 tumor cells within ascites and tumor. **c**, **d**, Representative plot (left) and tabulated data (right) for

404 glucose uptake (2-NBDG) (**c**) and mitochondrial activity (MitoTracker Deep Red) (**d**) of

405 EpCAM+CD45- tumor and EpCAM-CD45- stromal cells from ascites and tumor. **e**, Representative

406 gating strategy for CD25, CD137 and PD1 expression by flow cytometry. **f**, **g**, CD25, CD137 and PD1

407 expression on CD4+ T cells (**f**) and CD8+ T cells (**g**). **h**, **i**, Naive, central memory (Tcm), effector (Teff),

408 and effector memory (Tem) phenotype based on CCR7 and CD45RO expression. Representative plot

409 (left) and tabulated data (right) for CD4+ T cells (**h**) and CD8+ T cells (**i**) from ascites and tumor. P-

410 values (*p<0.05, **p<0.01, ***p<0.001) determined by paired t-test (**b-d, f-i**). Median Fluorescence
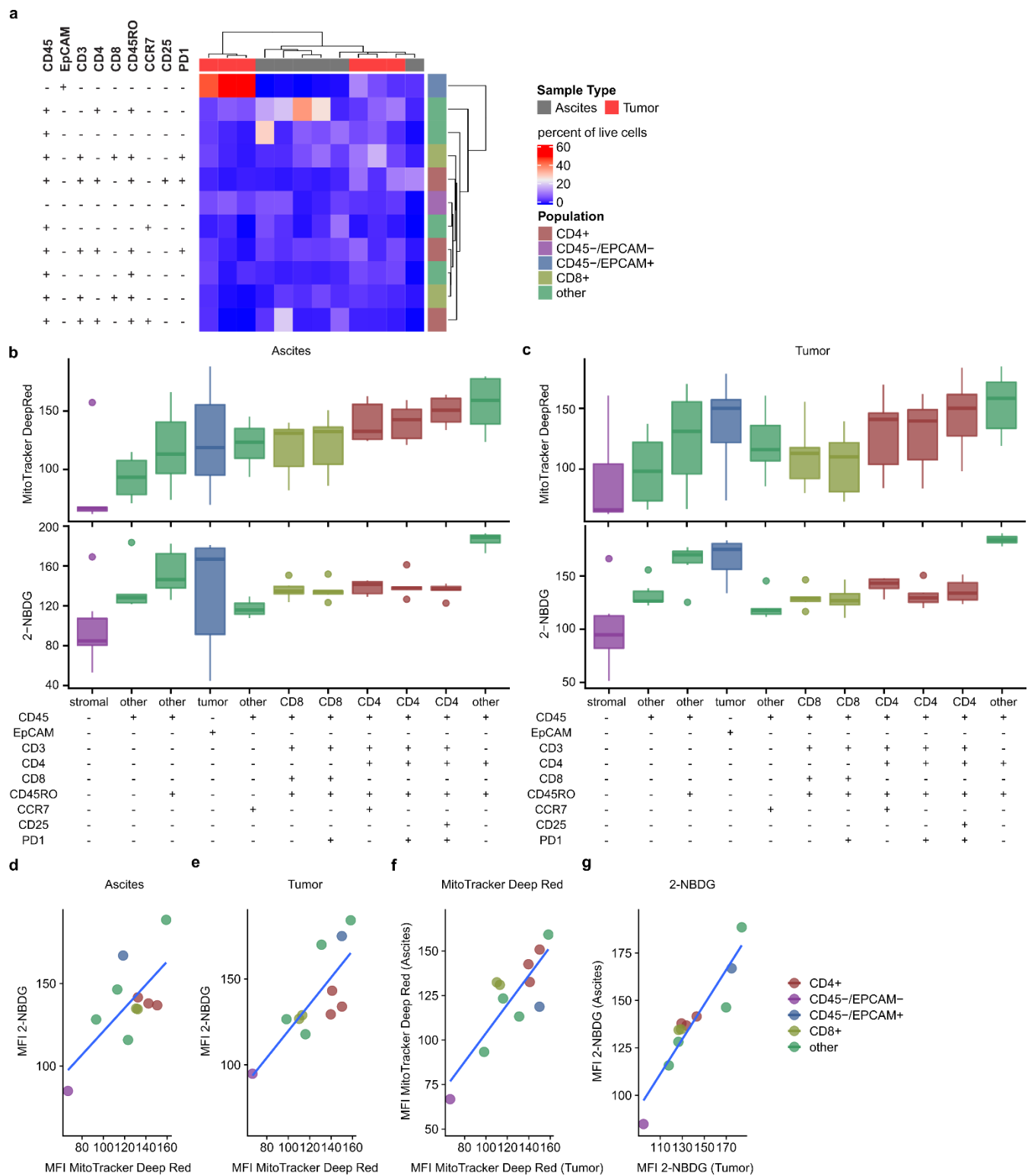
411 Intensity (MFI).
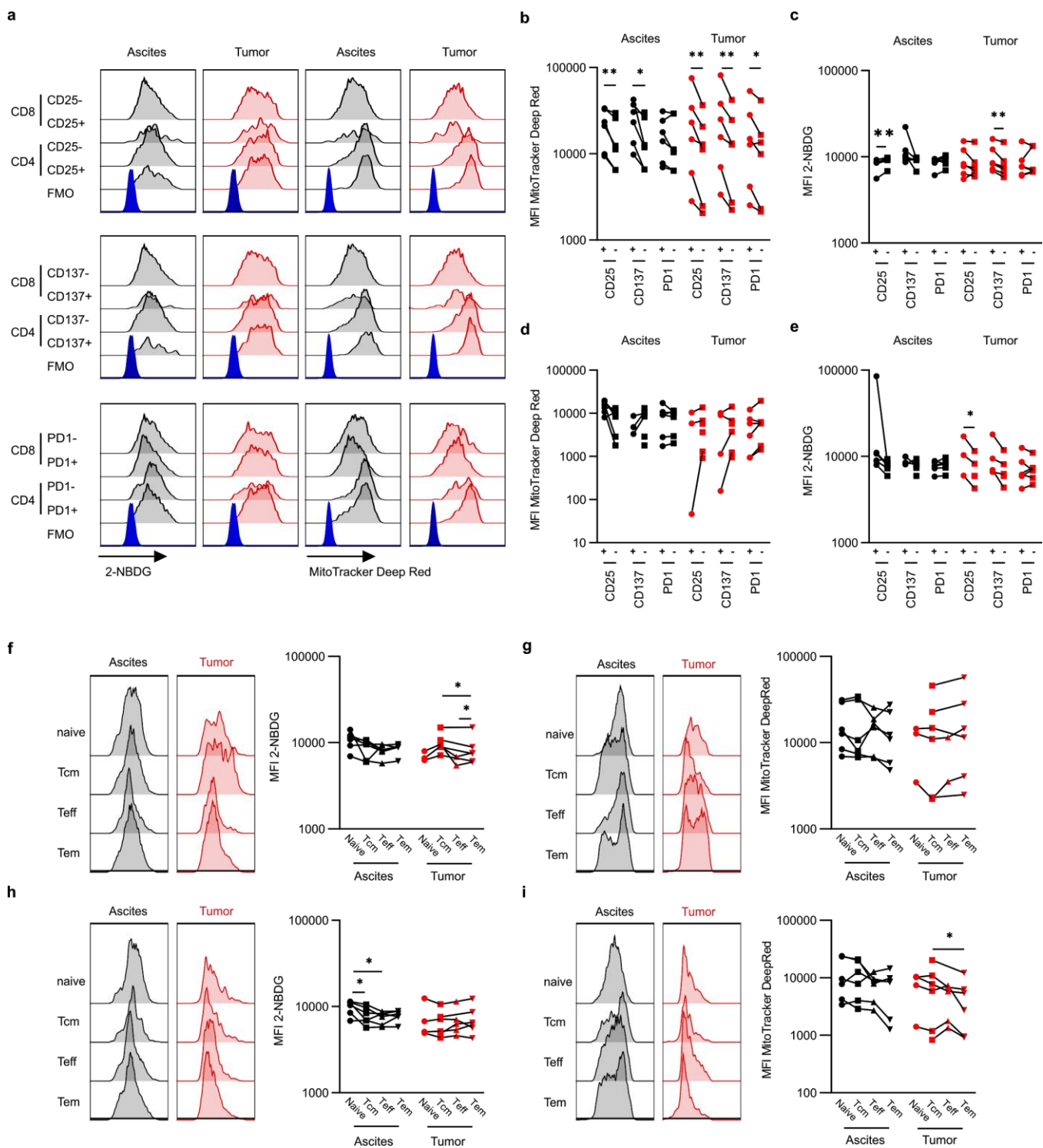
Extended Data Figure 2 | T cell metabolism is impacted by expression of activation markers. a,

Representative plots of glucose uptake (2-NBDG) and mitochondrial activity (MitoTracker Deep Red)

for CD25, CD137 and PD1 positive and negative CD4 and CD8 T cells. **b**, **c**, Mitochondrial activity (**b**)

and glucose uptake (**c**) of CD25, CD137 and PD1 CD4+ T cells. **d**, **e**, Mitochondrial activity (**d**) and

417   glucose uptake (**e**) of CD25, CD137 and PD1 CD8+ T cells. **f**, **g**, Representative plot (left) and tabulated

418   data (right) for glucose uptake (**f**) and mitochondrial activity (**g**) of naive, Tcm, Teff and Tem CD4+ T

419   cells. **h**, **i**, Representative plot (left) and tabulated data (right) for glucose uptake (**h**) and mitochondrial

420   activity (**i**) of naive, Tcm, Teff and Tem CD8+ T cells. P-values (*p<0.05, **p<0.01, ***p<0.001)

421   determined by paired t-test **b-i**). Lines indicate matched patients (**b-i**). Fluorescence Minus One (FMO);

422   Median Fluorescence Intensity (MFI); Central memory T cells (Tcm); Effector T cells (Teff); Effector

423   memory T cells (Tem).

Extended Data Figure 3 | Automated analysis of metabolism and cell type by flow cytometry. a, Heat map of cell type abundance. **b**, **c**, Glucose uptake and mitochondrial activity of cell fractions within ascites (**b**) and tumor (**c**). Boxplots show medians (lines), interquartile range (box hinges) and range of

428   data (box whiskers; excepting outliers, shown as points) **d, e**, Correlation between glucose uptake and

429   mitochondrial activity of cell fractions within the ascites (**d**) and tumor (**e**). **f, g**, Correlation of glucose

430   uptake (**f**) and mitochondrial activity (**g**) of cell fractions between ascites and tumor. Median (per

431   phenotype) of median (per sample) biexponential-transformed Median Fluorescence Intensity (MFI)

432   values shown.

a

b

c

433
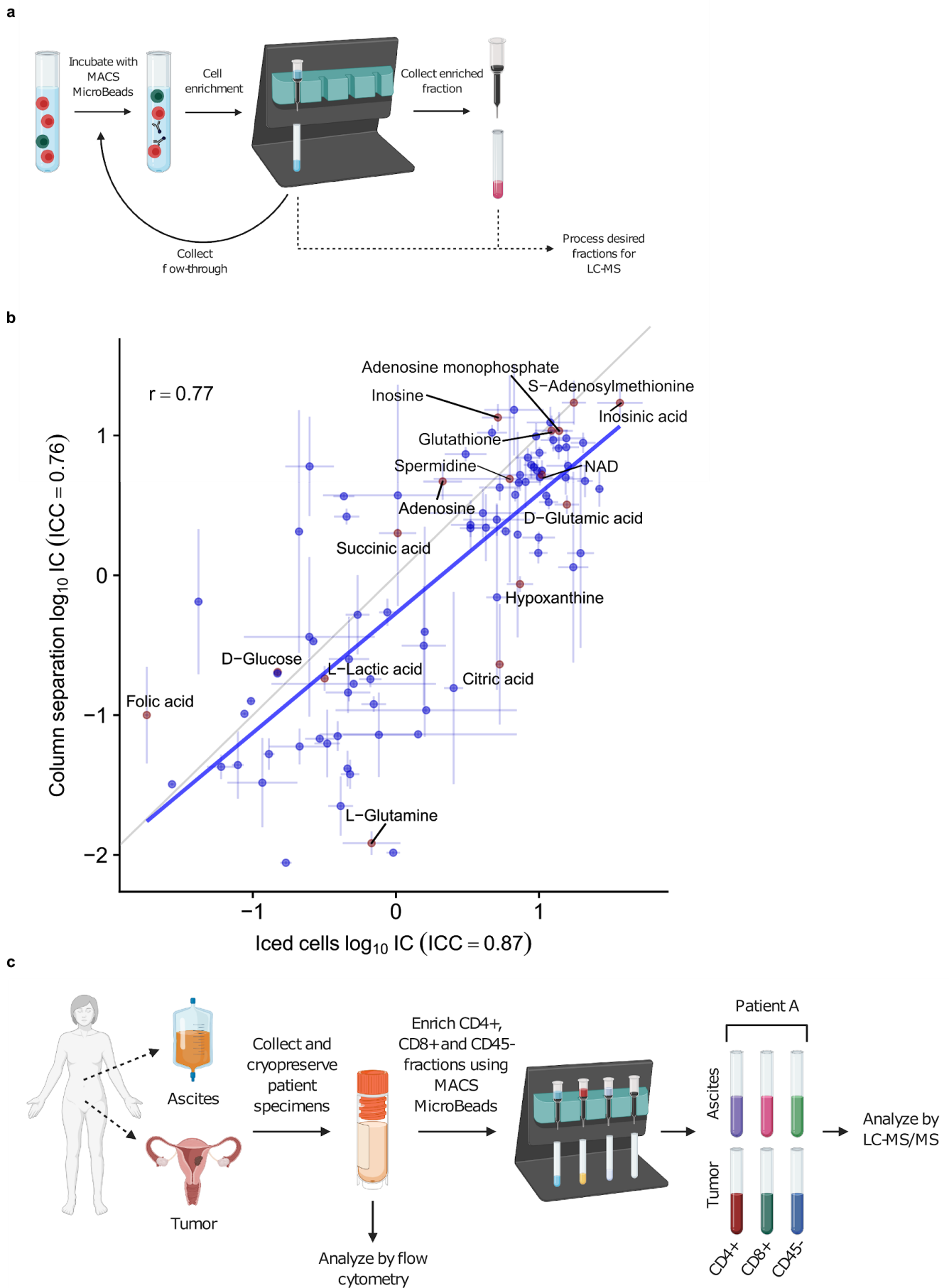
434   **Extended Data Figure 4 | Schematic workflow and impact of enrichment on metabolite profiling.**

435   **a**, Schematic of magnetic bead enrichment. Cells underwent three consecutive rounds of magnetic bead

436   enrichment or remained on ice. **b**, Impact of enrichment type on metabolite abundance. Means of

437   triplicate measurements for each enrichment type +/- SE shown. Gray line represents 1:1 relationship.

438   Intraclass correlation for replicate measurements (ICC) shown in axis labels. **c**, Schematic of patient

439   metabolite profiling workflow. Ascites or tumor was collected from patients and cryopreserved. A

440   fraction of each sample was analyzed by flow cytometry, while the remaining sample underwent three

441   rounds of enrichment for CD4+, CD8+ and CD45- cells. These cell fractions were analyzed using LC-

442   MS/MS.
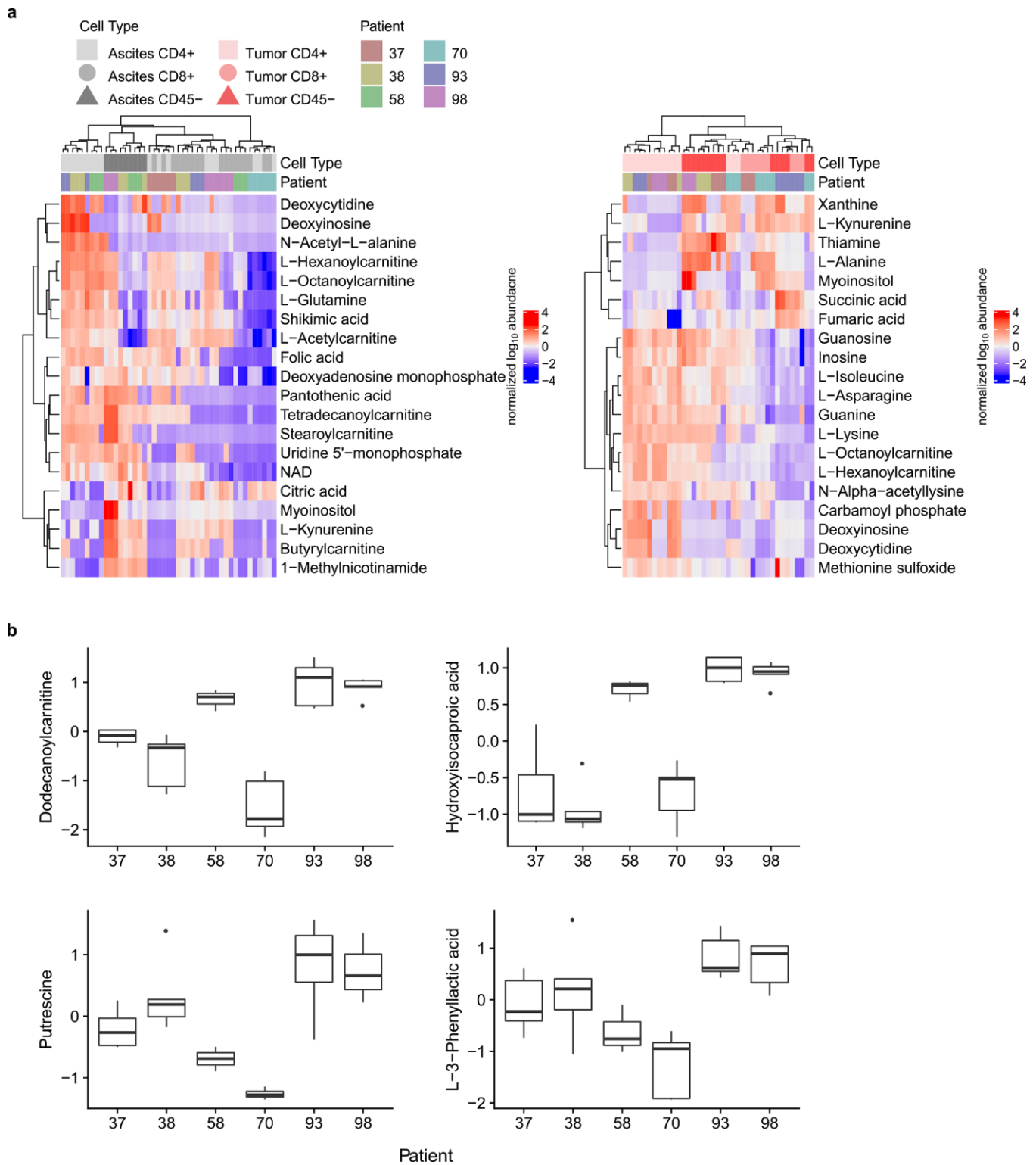
Extended Data Figure 5 | Changes in relative metabolite abundance across cell types within ascites and tumor. a, Heatmap of normalized metabolite abundance, with dendrograms representing Ward's clustering of Euclidean distances among samples. Relative abundance of metabolites in the ascites (left)

447 and tumor (right). **b,** Top four significantly differing metabolites across patients (all P_{adj} for F-Test of

448 patient effect in *limma* < 0.05). Boxplots show medians (lines), interquartile range (box hinges) range of

449 data up to 1.5X interquartile range (box whiskers; excepting outliers, shown as points).

450
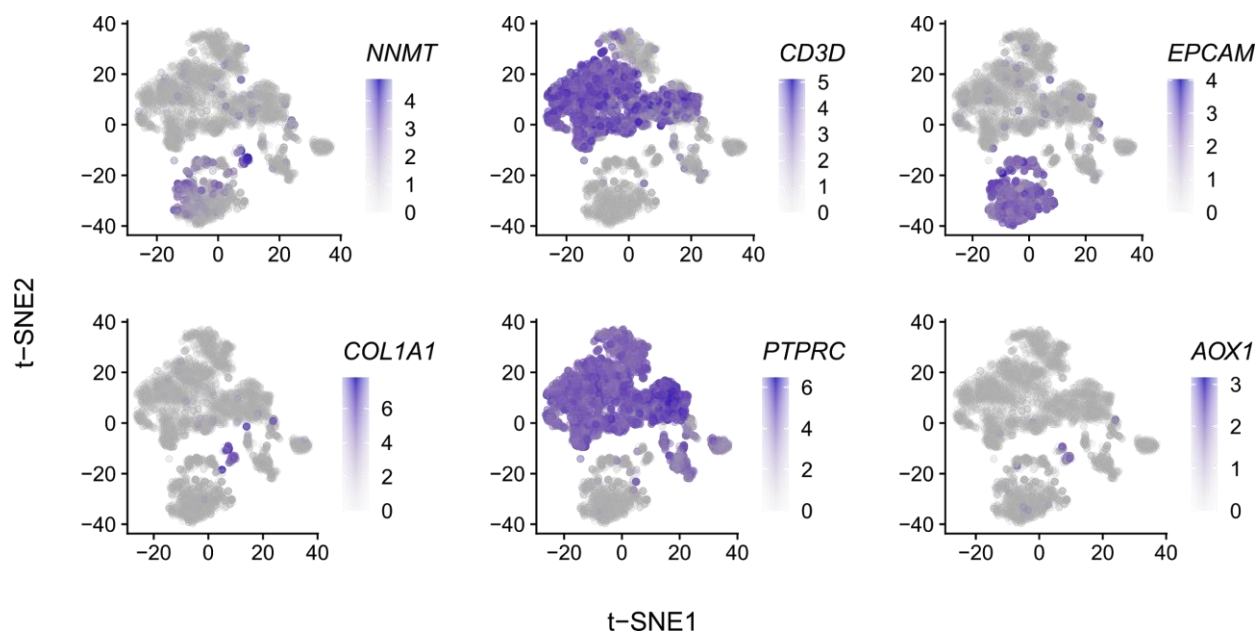
**Extended Data Figure 6 | Expression of population defining makers and metabolic genes within

452 the scRNA-seq data.** Expression of *NNMT, CD3D*, *EPCAM*, *COL1A1*, *PTPRC* and *AOX1* within

453 ascites and tumor, shown as $\log_2$ normalized unique molecular identifier (UMI) counts.

454
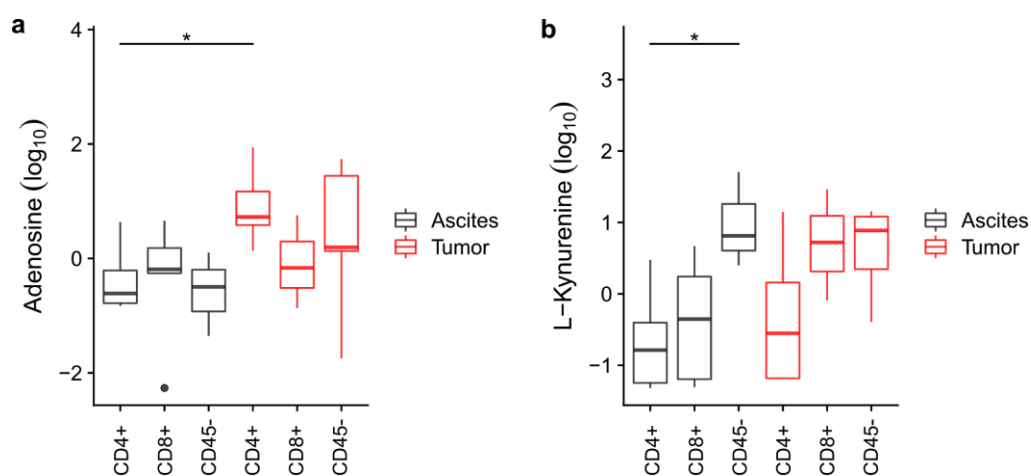
**Extended Data Figure 7 | Relative abundance of adenosine (a) and L-kynurenine (b) measured by

456 LC-MS/MS.** P-values determined as described in methods (*p$<$0.05). Boxplots show medians (lines),

457 interquartile range (box hinges) and range of data up to 1.5X interquartile range (box whiskers; outliers

458 shown as points). P values determined using *limma* as per Figure 3.

459

460 **Extended Data Table 1 | HGSC patient characteristics for metabolic profiling by flow cytometry**

461 **and LC-MS/MS**.

Patient	Tumor location	Age at surgery	Survival (months)[*]	Tumor stage[†]	Tumor grade[†]	Ascites volume (mL)
37	omentum	70	12	3C	3	1800
38	ovary	40	16	T3b	3	1200
70	omentum	50	23	3C	3	80
58	omentum	78	18	4	3	2000
93	fallopian tube	53	82	3B	2	1600
98	omentum	39	13	3C	3	2000

462 [*] Survival calculated from the date of diagnosis to the date of death

463 [†] Tumor stage and grade were determined by a pathologist at the time of surgery

464

465 **Extended Data Table 2 | Flow cytometry metabolic profiling panel.**

Fluorochrome	Marker	Expression	Clone	Company	Catalogue number
---	2-NBDG	Glucose uptake	---	Thermo	N13195
PE	CD326 (EpCAM)	Epithelial cells	1B7	Thermo	12-9326-42
PerCP	CD8	Effector T cells	RPA-T8	Biolegend	301030
PerCP-eFluor710	CD25	Activation/Tregs	4E3	Thermo	46-0257-41
PE-Cy7	CD45RO	Phenotype	UCHL1	Thermo	25-0457-42
---	MitoTracker Deep Red	Mitochondrial activity	---	Thermo	M22426
AF700	CD4	Helper T cells	RPA-T4	Biolegend	300526
APC/Fire750	CCR7	Phenotype	G043H7	Biolegend	353246
eFlour506	Viability	Live/dead cells	---	Thermo	65-0866-14
PO	CD45	Leukocytes	HI30	Thermo	MHCD4530
BV605	CD137	Activation	4B4-1	Biolegend	309822
BV650	CD279 (PD1)	Activation/Exhaustion	EH12.2H7	Biolegend	329950
BV750	CD3	T cells	SK7	Biolegend	344845

466
467

468 **Extended Data Table 3 | HGSC patient characteristics for single cell RNA sequencing.**

Patient	Tumor location	Age at surgery	Survival (months)[*]	Tumor stage[†]	Tumor grade[†]
46	ovary	54	24	3C	3
58	omentum	78	18	4	3
59	omentum	68	26	3C	3
69	omentum	59	17	3C	3
109	ovary	77	62	3C	3

469 * Survival calculated from the date of diagnosis to the date of death

470 † Tumor stage and grade were determined by a pathologist at the time of surgery